J. Fluid Mech. (2009), *vol.* 635, *pp.* 361–388.
doi:10.1017/S0022112009007599

Numerical simulations of lock-exchange compositional gravity current

SENG KEAT OOI, GEORGE CONSTANTINESCU† AND LARRY WEBER

Civil and Environmental Engineering, IIHR-Hydroscience and Engineering,
C. Maxwell Stanley Hydraulics Laboratory, University of Iowa,
Iowa City, IA 52242, USA

(Received 15 September 2008; revised 6 April 2009; accepted 10 April 2009)

Compositional gravity current flows produced by the instantaneous release of a finite-volume, heavier lock fluid in a rectangular horizontal plane channel are investigated using large eddy simulation. The first part of the paper focuses on the evolution of Boussinesq lock-exchange gravity currents with a large initial volume of the release during the slumping phase in which the front of the gravity current propagates with constant speed. High-resolution simulations are conducted for Grashof numbers $\sqrt{Gr} = 3\,150$ (LGR simulation) and $\sqrt{Gr} = 126\,000$ (HGR simulation). The Grashof number is defined with the channel depth h and the buoyancy velocity $u_b = \sqrt{g'h}$ (g' is the reduced gravity). In the HGR simulation the flow is turbulent in the regions behind the two fronts. Compared to the LGR simulation, the interfacial billows lose their coherence much more rapidly (over less than $2.5h$ behind the front), which results in a much faster decay of the large-scale content and turbulence intensity in the trailing regions of the flow. A slightly tilted, stably stratified interface layer develops away from the two fronts. The concentration profiles across this layer can be approximated by a hyperbolic tangent function. In the HGR simulation the energy budget shows that for $t > 18h/u_b$ the flow reaches a regime in which the total dissipation rate and the rates of change of the total potential and kinetic energies are constant in time. The second part of the paper focuses on the study of the transition of Boussinesq gravity currents with a small initial volume of the release to the buoyancy–inertia self-similar phase. When the existence of the back wall is communicated to the front, the front speed starts to decrease, and the current transitions to the buoyancy–inertia phase. Three high-resolution simulations are performed at Grashof numbers between $\sqrt{Gr} = 3 \times 10^4$ and $\sqrt{Gr} = 9 \times 10^4$. Additionally, a calculation at a much higher Grashof number ($\sqrt{Gr} = 10^6$) is performed to understand the behaviour of a bottom-propagating current closer to the inviscid limit. The three-dimensional simulations correctly predict a front speed decrease proportional to $t^{-\alpha}$ (the time t is measured from the release time) over the buoyancy–inertia phase, with the constant α approaching the theoretical value of $1/3$ as the current approaches the inviscid limit. At Grashof numbers for which $\sqrt{Gr} > 3 \times 10^4$, the intensity of the turbulence in the near-wall region behind the front is large enough to induce the formation of a region containing streaks of low and high streamwise velocities. The streaks are present well into the buoyancy–inertia phase before the speed of the front decays below values at which the streaks can be sustained. The formation of the velocity streaks induces a streaky distribution of the bed friction velocity in the region immediately behind the front. This distribution becomes finer as the Grashof

† Email address for correspondence: sconstan@engineering.uiowa.edu

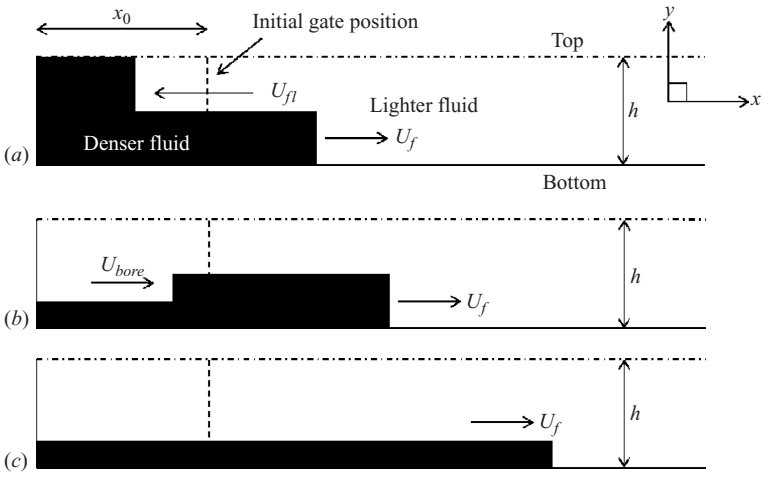

FIGURE 1. Sketch of a finite-volume lock-exchange flow in a channel. (*a*) Lock release flow immediately after the gate is removed with associated front velocities of the heavier (U_f) and lighter (U_{fl}) currents. (*b*) Gravity current after the bore has formed. The bore velocity is U_{bore}. (*c*) Gravity current during the buoyancy–inertia phase.

number increases. For simulations in which the only difference was the value of the Grashof number ($\sqrt{Gr} = 4.7 \times 10^4$ versus $\sqrt{Gr} = 10^6$), analysis of the non-dimensional bed friction velocity distributions shows that the capacity of the gravity current to entrain sediment from the bed increases with the Grashof number. Past the later stages of the transition to the buoyancy–inertia phase, the temporal variations of the potential energy, the kinetic energy and the integral of the total dissipation rate are logarithmic.

1. Introduction

Gravity currents are mainly horizontal flows moving under the influence of gravity and generated by density differences within a fluid or between two fluids. Predicting and understanding the evolution of gravity currents is of considerable interest to many applications in engineering and geophysics (e.g. see Fanneløp 1994; Simpson 1997). Gravity currents can be generated by the instantaneous removal of a vertical lock gate separating two fluids at rest (figure 1*a*) and of different densities in a channel (lock-exchange flow). The lock-exchange flow is dominated by two instabilities: the predominantly two-dimensional Kelvin–Helmholtz (KH) instability at the interface between the heavier and the lighter fluid and the three-dimensional lobe-and-cleft instability at the front. A large number of experimental and theoretical studies were conducted to isolate the various mechanisms that drive gravity currents in lock-exchange flows and predict the temporal evolution of global parameters such as the front velocity and the height of the head region. The case of low-density differences, where the Boussinesq approximation is valid, was considered in many studies (Simpson 1972; Britter & Simpson 1978; Simpson & Britter 1979; Huppert & Simpson 1980; Huppert 1982; Keller & Chyou 1991; Hallworth *et al.* 1996; Shin, Dalziel & Linden 2004).

In the geometrical set-up considered in the present numerical study, the horizontal channel is straight and has a rectangular section. A rear wall is present at one end of the straight channel. The heavier lock fluid initially occupies the volume between the rear wall and the lock gate (figure 1*a*). When the lock gate is removed instantaneously, a bottom current containing heavier lock fluid forms. This case was studied experimentally and analytically by, among others, Huppert & Simpson (1980), Rottman & Simpson (1983), Choi & Garcia (1995), Hacker, Linden & Dalziel (1996) and Shin *et al.* (2004). In this paper we limit our investigation to compositional currents in which density differences are produced by a difference in a property of the fluid (e.g. temperature or salinity), and these differences are small enough for the Boussinesq approximation to be valid. We study only the full-depth release case in which the initial height of the lock fluid is equal to the channel height h.

Detailed measurements of the velocity and density fields within the gravity current are seldom available from experimental studies. Additionally, in many applications involving turbidity currents or compositional currents propagating over loose beds, information on the spatial and temporal distributions of the bed shear stress is essential to determine the amount of sediment entrained and carried by the current. Measurements of the instantaneous bed shear stress distribution are nearly impossible to achieve experimentally. This kind of information can be used in simpler models that try to predict the sediment entrained by the current in an integral sense and to qualitatively understand the way the sediment is entrained. Finally, information on the global energy balance at different stages of the evolution of the current are quite difficult to obtain experimentally. High-resolution numerical simulations can provide this information.

A three-dimensional numerical simulation of a Boussinesq lock-exchange flow in a long channel was reported by Härtel, Carlsson & Thunblom (2000*a*) and Härtel, Meiburg & Necker (2000*b*), who performed direct numerical simulation (DNS) at a relatively low Grashof number ($\sqrt{Gr} = 3\,450$). The simulation successfully captured the formation of the lobe-and-cleft instability at the front of the gravity current and allowed a detailed investigation of the flow topology in the head region. Three-dimensional DNSs at Grashof numbers higher than the one considered by Härtel *et al.* (2000*b*) were reported by Cantero *et al.* (2007) in planar and cylindrical configurations. Hallez & Magnaudet (2008) used DNS to investigate the role of confinement and channel geometry on the evolution of lock-exchange gravity current flows.

In the present work a large eddy simulation (LES) code (Pierce & Moin 2001; Chang, Constantinescu & Park 2006, 2007; Ooi, Constantinescu & Weber 2007*a*, 2007*b*) is used to perform the numerical simulations. High-resolution three-dimensional LESs can resolve the dynamically important eddies in the flow, similar to DNS, but are computationally much less expensive at high Grashof numbers. For example a three-dimensional DNS at $\sqrt{Gr} \cong 10^5$ would require an increase of the number of mesh points by at least one order of magnitude compared to the mesh used in a three-dimensional LES. The LES solver uses a non-dissipative method and a dynamic Smagorinsky subgrid-scale (SGS) model to account for the effect of the unresolved scales. The use of a dynamic procedure (Lilly 1992) allows to estimate the eddy viscosity and eddy diffusivity based on the flow physics (information from the smallest resolved scales) and to reduce to a minimum the dissipation added to the resolved scales. This means that the resolved scales can be computed accurately. Compared to well-resolved DNS, in which all the scales up to the dissipative range are resolved by the simulation, LES contains a certain amount of empiricism related to

the use of an SGS model. Still, LES with a dynamic SGS model offers one of the best alternatives for the study of the physics of high-Grashof-number gravity currents. As two-dimensional highly resolved DNSs or LESs are in most cases about two orders of magnitude less expensive than three-dimensional highly resolved simulations in terms of the required computational resources, we think it is important to assess their abilities to predict high-Grashof-number lock-exchange flows. Results in § 4.1 will show that two-dimensional simulations are of limited use in studying high-Grashof-number currents ($\sqrt{Gr} > 10^4$) in the later stages of their evolution. This is the reason why in this study three-dimensional simulations are used to investigate the flow physics of high-Grashof-number currents.

In the first part of the paper we focus on the case in which the initial aspect ratio of the lock fluid $R = h/x_0$ (x_0 is the distance between the rear wall and the lock gate) is much smaller than one (initial volume of release is large) and the channel is long enough to avoid interactions of the gravity currents with the endwalls (figure 1*a*). We investigate the evolution of lock-release gravity currents at relatively large Grashof numbers during the short initial acceleration phase and during the slumping phase in which the front velocity of the current U_f can be considered constant. The non-dimensional front velocity expressed as Froude number $Fr_f = U_f/u_b$ ($u_b = \sqrt{g'h}$ is the buoyancy velocity and g' is the reduced gravity) is dependent on the Grashof number which is related to the ratio of buoyancy forces to viscous forces. The square root of the Grashof number $\sqrt{Gr} = u_b h/\nu$ (ν is the molecular viscosity and h is the channel depth) plays the role of a Reynolds number. Simulations are performed at two Grashof numbers. The set-up of the simulations (e.g. no-slip boundary condition at the top and bottom surfaces, Schmidt number) is chosen to be identical to that in the three-dimensional DNS study of Härtel *et al.* (2000*b*). In the first simulation, denoted LGR ($\sqrt{Gr} = 3\,150$), the turbulence in the region behind the front is weak. In the second simulation, denoted HGR ($\sqrt{Gr} = 126\,000$), the flow in the region behind the front is strongly turbulent. We consider the gravity current highly turbulent if velocity spectra contain a clear inertial range as the upstream part to the current is convected over streamwise locations situated at a sufficient distance from the lock gate ($\cong 4h$ in the HGR simulation).

In the second part of the paper we consider the case of gravity currents generated by a small initial volume of release ($R = O(1)$) and focus on the evolution of the heavier (forward-propagating in figure 1) current after the lighter (backward-propagating) current forming along the top of the channel starts interacting with the rear wall. As the lighter current starts interacting with the rear wall, it reflects and forms a bore (figure 1*b*) that propagates in the same direction as the heavier current. The bore speed U_{bore} is nearly constant and slightly higher than the front velocity (U_f). Meanwhile, the head of the heavier current propagates with practically constant depth and constant velocity (U_f). For sufficiently high Grashof numbers, once the bore catches the front (figure 1*c*), the heavier current transitions to the buoyancy–inertia self-similar phase in which the motion of the current is determined by a balance between the inertial and gravitational (buoyancy) forces, and the front velocity decays with time following a power law ($U_f \sim t^{-1/3}$). If the channel is long enough, such that viscous effects become dominant, the current will transition to the viscous–buoyancy self-similar phase in which the motion of the current is determined by a balance between the viscous and gravitational forces. The flow at the front decelerates faster as $U_f \sim {}^{-4/5}$ (see Huppert 1982; Rottman & Simpson 1983). The buoyancy–inertia phase may not be present if the Grashof number is sufficiently low (Rottman & Simpson 1983; Cantero *et al.* 2007).

Case	$\sqrt{Gr}$	L_1/h	Aspect ratio, $R = h/x_0$
A	30 980	18	0.67
B	87 750	9	1.00
CL	47 750	13.483	1.78
CH	1.0×10^6	13.483	1.78
D	530	18	1.00

TABLE 1. Details of finite-volume lock-exchange simulations with $R = O(1)$.

	Experiment		Simulation		Bore overtakes the front		
Case	Re_f	Fr_f	Re_f	Fr_f	Location, x/h	Time, t/t_0	$l = (x_f - x_0)/x_0$
A	7000	0.45 ± 0.01	6890 (6820)	0.44	9.9 (10.4)	9.7 (10.2)	5.6 (5.9)
B	19 700	0.45 ± 0.01	19 750 (19 730)	0.45	–	–	–
CL	11 000	0.46 ± 0.01	10 875 (10 755)	0.45	5.5 (5.9)	11.5 (12.5)	8.8 (9.5)
CH			248 000	0.485	5.5	10.0	8.8
D			98	0.37	(10.1)	(27.4)	(10.1)

TABLE 2. Summary of simulation results with $R = O(1)$. The values in parenthesis are from two-dimensional simulations.

The set-up of the numerical test cases considered in the second part of the paper was inspired by the experimental study of Hacker *et al.* (1996) who investigated the effect of the initial aspect ratio of the lock fluid, R, on the evolution of lock-exchange currents. Four three-dimensional LESs denoted A ($R = 0.67$), B ($R = 1$), CL ($R = 1.78$) and CH ($R = 1.78$) are performed at $\sqrt{Gr} = 30\,980$, 87 750, 47 750 and 10^6, respectively (see table 1). The Grashof numbers in cases A, B and CL are in the range in which most experimental studies are conducted ($\sqrt{Gr} = 10^4$–10^5). Comparison of cases A, B and CL serves to better understand the effect of R on the transition to the buoyancy–inertia phase. Among the well-resolved three-dimensional simulations, case B has the highest Grashof number and is used to illustrate the structure of the near-bed flow in the region in which the flow inside the current is strongly turbulent. However, as the computational domain length and conditions in case B are such that they do not allow a detailed study of the evolution of the current during the buoyancy–inertia phase, most of the discussion focuses on case CL (see table 2) which is used to investigate the evolution of the current after the end of the transition to the buoyancy–inertia phase. The geometry and flow conditions in cases CL and CH are identical except for the value of the Grashof number. Case CH allows to better understand the physics of finite-volume lock-release currents for flow conditions that are closer to the inviscid state that is often assumed in theoretical models and to conditions encountered in engineering and geoscience applications. The required computing time for a well-resolved three-dimensional DNS of case CH would be close to three orders of magnitude larger than the one for LES. This is well outside the reach of today's supercomputers. Finally, a two-dimensional simulation (case D) at a low Grashof number ($\sqrt{Gr} = 530$, $R = 1$) is performed to study the evolution of a current that transitions directly from the slumping phase to the viscous–buoyancy phase. This is an acceptable approximation, as, based on experimental observations (e.g. Simpson 1997), the behaviour of low-Grashof-number gravity currents is quasi-two-dimensional.

The numerical method and the set-up of the numerical simulations are discussed in § 2. The same section discusses the effect of the Schmidt number. Section 3 focuses on the evolution of lock-exchange flows with $R \ll 1$ during the slumping phase. The effect of the Grashof number and the energy budget are analysed in §§ 3.1 and 3.2, respectively. Section 4 focuses on the evolution of lock-exchange flows with $R = O(1)$. Grashof number effects on the development of flow instabilities and current evolution are analysed in § 4.1. Section 4.2 discusses the energy budget and the streamwise distribution of the dissipation rate. Section 4.3 analyses the temporal variation of the front velocity. The effect of the Grashof number on the near-bed flow structure and the bed friction velocity distributions induced by the passage of a gravity current after the bore has formed is investigated in § 5. Section 6 presents the main conclusions.

2. Description of numerical model and simulations

The filtered continuity and momentum equations and the advection–diffusion equation for the concentration $\bar{C}$ are made dimensionless using the channel depth, h, and the buoyancy velocity, $u_b = \sqrt{g'h}$, ($g' = g(\bar{C}_{max} - \bar{C}_{min})/\bar{C}_{max}$, where $\bar{C}_{max}$ and $\bar{C}_{min}$ are the maximum and minimum initial concentrations in the domain and g is the gravitational acceleration):

$$\frac{\partial u_i}{\partial x_i} = 0, \tag{1}$$

$$\frac{\partial u_i}{\partial t} + \frac{\partial (u_i u_k)}{\partial x_k} = -\frac{\partial p}{\partial x_i} + \frac{\partial}{\partial x_k}\left[\left(\frac{1}{\sqrt{Gr}} + \nu_{SGS}\right)\left(\frac{\partial u_i}{\partial x_k} + \frac{\partial u_k}{\partial x_i}\right)\right] - C\delta_{i2}, \tag{2}$$

$$\frac{\partial C}{\partial t} + \frac{\partial (C u_k)}{\partial x_k} = \frac{\partial}{\partial x_k}\left(\left(\frac{1}{\sqrt{Gr}\,Sc} + \alpha_{SGS}\right)\frac{\partial C}{\partial x_k}\right), \tag{3}$$

where p and u_i are the dimensionless pressure and Cartesian velocity component in the i direction. The dimensionless concentration is defined as $C = (\bar{C} - \bar{C}_{min})/(\bar{C}_{max} - \bar{C}_{min})$ and is linearly related to the density ρ. The coordinates in the three directions are denoted either (x_1, x_2, x_3) in index notation or (x, y, z). The vertical direction is y ($i = 2$, in index notation). The time scale is $t_0 = h/u_b$.

The Schmidt number Sc is the ratio of the molecular viscosity ν to the molecular diffusivity κ. The expressions used to calculate the SGS viscosity (ν_{SGS}) and SGS diffusivity (α_{SGS}) in (2) and (3) can be found in Pierce & Moin (2001). No assumptions are needed of the value of the turbulent Schmidt number, as the dynamic procedure (Germano *et al.* 1991) directly estimates the value of the SGS diffusivity based on the resolved velocity and concentration fields. The need to use empirical near-wall viscosity corrections (e.g. Van Driest damping functions) is avoided when the dynamic procedure is used and the governing equations are integrated through the viscous sublayer ($\Delta n_1^+ \cong 1$ for the first point off the wall, where $n^+ = n u_\tau/\nu$, u_τ is the wall friction velocity and n is the distance from the wall). The simulations discussed in the present paper were conducted with a ratio of the test filter to the grid filter equal to two (Pierce & Moin 2001).

The numerical solver is a finite-volume DNS/LES code (see Pierce & Moin 2001, 2004). The conservative form of the Navier–Stokes equations is integrated on non-uniform Cartesian meshes. A semi-implicit iterative method that employs a staggered conservative space–time discretization is used to advance the equations in time while ensuring second-order accuracy in both space and time. A Poisson equation is solved

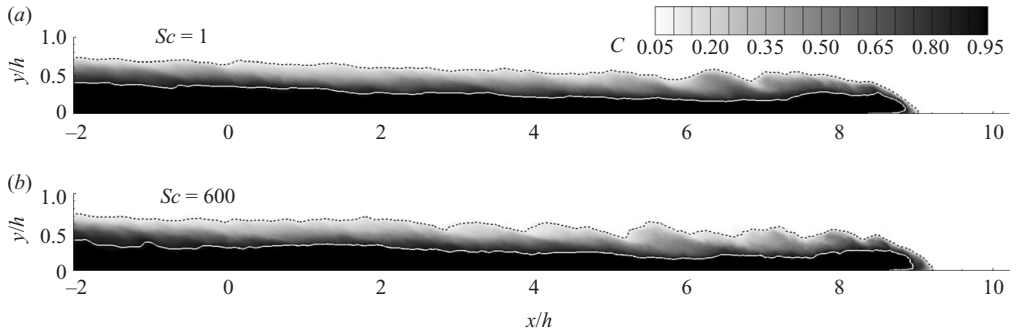

FIGURE 2. Visualization of the lock-exchange flow in case HGR ($\sqrt{Gr} = 126\,000$) using spanwise-averaged concentration contours. (*a*) Three-dimensional simulation, $Sc = 1$; (*b*) three-dimensional simulation, $Sc = 600$. The solid and dashed lines correspond to the $C = 0.9$ and $C = 0.1$ concentration levels, respectively.

for the pressure using a multigrid algorithm. The algorithm discretely conserves energy (Mahesh, Constantinescu & Moin 2004), which allows obtaining solutions at high Grashof numbers in the LES regime without artificial damping. All operators are discretized using central discretizations, except the convective term in the advection–diffusion equation solved for the concentration, for which the QUICK scheme (Pierce & Moin 2001) is used.

In the simulations with $R \ll 1$ the top and bottom surfaces were simulated as no-slip smooth walls. The length of the computational domain was $L_1 = 24h$, which is long enough to prevent interaction of the currents with the lateral boundaries for $t < 25t_0$. Consequently, the velocity was assumed to be equal to zero at the two endwall boundaries. The grid size was $2048 \times 80 \times 160$ in the streamwise, spanwise (domain width $L_3 = 1.5h$) and vertical directions ($L_2 = h$), respectively. Away from the walls the grid spacing in the three directions was $0.01h$–$0.02h$. To resolve the viscous sublayer, the grid spacing in the vertical direction was reduced to $0.0005h$ near the walls. A zero normal gradient was imposed for the concentration at the top, bottom and endwall boundaries.

In most of the simulations with $R \ll 1$ we assumed a unity value for the Schmidt number, such that a direct comparison with the results reported by Härtel *et al.* (2000*b*) is possible. Härtel *et al.* (2000*b*), Necker *et al.* (2005) and Cantero *et al.* (2007) found that the value of the Schmidt number does not significantly alter the generality of the results as long as it is of order one or larger. To confirm this, two three-dimensional simulations of the HGR case ($\sqrt{Gr} = 126\,000$), one with $Sc = 1$ and the other with $Sc = 600$, were conducted. Results showed the front speed was identical in the two simulations, while the shape and structure of the gravity current behind the front were similar at all stages of the evolution of the current. The sample results in figure 2 confirm the small effect of the Schmidt number on the evolution of high-Grashof-number currents. In part, this is because α_{SGS} is significantly larger than the molecular diffusivity in the regions of strong turbulence even for $Sc = 1$.

All three-dimensional simulations with $R = O(1)$ were run with $Sc = 600$, corresponding to saline diffusion in water. This is because one of our goals was to compare the simulation results with the corresponding experiments of Hacker *et al.* (1996) that were performed using saline water. Preliminary two-dimensional simulations conducted with $1 < Sc < 600$ for case CL ($R = 1.78$) did not find a significant effect of the Schmidt number on the solution. To mimic the presence

of the free surface in the experimental set-up of Hacker *et al.* (1996), the top surface of the channel was treated as a non-deformable slip boundary (zero shear stress in the horizontal direction and zero vertical velocity) rather than as a no-slip wall as in the simulations with $R \ll 1$. This is justified, as in all the test cases the Froude number $U_f/\sqrt{gh}$ was much smaller than 0.5, which indicates negligible free-surface deformations. A convective outflow boundary condition (Pierce & Moin 2001) of the form $\partial F/\partial t + U_c \partial F/\partial x = 0$ (F is a velocity component or the concentration) was used at the right endwall. The value of the convective velocity U_c was equal to the estimated front velocity when reaching the right endwall.

In simulations A, B, CL and CH, the Reynolds number Re_f, defined with the constant front velocity before the bore overtakes the front and the channel half-depth, is in the range 7000–248 000 (table 2). The size of the grid was $3072(x) \times 160(y) \times 72(z)$. The grid spacing and the degree of clustering of the mesh points in the surface-normal direction at the bottom and endwalls were similar to the ones in the simulations with R$\ll$ 1. For case CH the stretching in the wall-normal direction was somewhat larger, to insure $\Delta n^+ \cong 2$ for the first row of points off the walls. In the two-dimensional simulations the size of the grid was $3072(x) \times 160(y)$. The reduction in the computational resources needed to perform the two-dimensional simulations is of the order of the ratio between the grid sizes in the corresponding three-dimensional and two-dimensional simulations. In case D ($\sqrt{Gr} = 530,\ Re_f = 98$) the flow is laminar and quasi-two-dimensional. A two-dimensional simulation of case D was performed.

Similar to the investigations of Härtel *et al.* (2000*b*), Necker *et al.* (2005) and Cantero *et al.* (2007), the flow was assumed to be periodic in the spanwise direction in all the three-dimensional simulations. Thus, the present study considers only gravity currents of large relative width that are particularly relevant for geoscience applications. The effect of the sidewalls was studied by Hallez & Magnaudet (2008). The non-dimensional concentration field was initialized with a constant value of one in the region containing the lock fluid and a constant value of zero in the rest of the computational domain. A random disturbance was applied to the concentration field in the lock-gate region to accelerate the growth of three-dimensional instabilities. The time step in the simulations was $0.001t_0$.

3. Gravity currents with a large volume of release ($R \ll 1$)

The main focus of this section is the study of full-depth release gravity currents with $R \ll 1$ at Grashof numbers that are high enough to produce a strongly turbulent flow behind the front. A main question we try to answer in this section is whether the presence of a strongly turbulent flow behind the front induces significant changes in the structure of the gravity current with respect to that observed for currents with $\sqrt{Gr} < 10^4$ that were previously studied using three-dimensional DNS.

3.1. *Role of the Grashof number*

The flow in the lower-Grashof-number three-dimensional simulation at $\sqrt{Gr} = 3\,150$ is illustrated in figure 3(*a*) using spanwise-averaged concentration isocontours. The flow evolution is similar to the one described by Härtel *et al.* (2000*b*). The flow is highly three-dimensional only in the front region in which lobes and clefts develop once the head has formed. Quasi-two-dimensional interfacial billows are generated behind the front. The evolution of the backward- and forward-propagating currents is very close to antisymmetrical. By contrast, in the higher-Grashof-number simulation at $\sqrt{Gr} = 126\,000$ (e.g. see figure 3*b*) the break in the antisymmetry of the evolution of

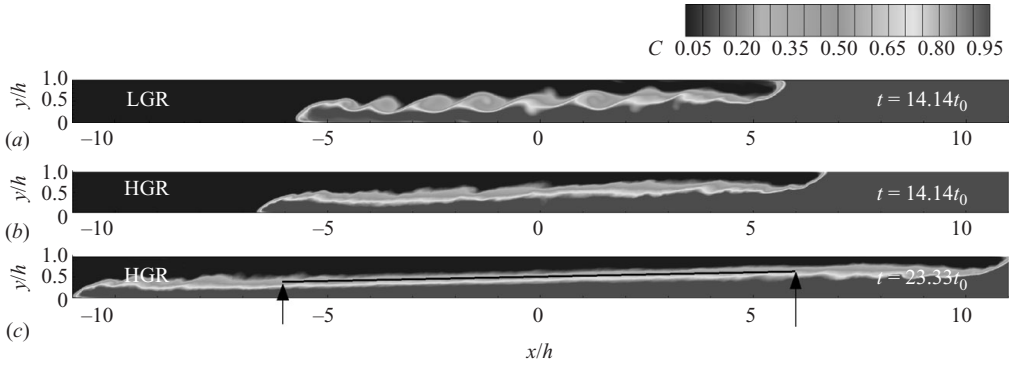

FIGURE 3. Visualization of the lock-exchange flow in three-dimensional simulations with $R \ll 1$ using spanwise-averaged concentration contours. (*a*) Case LGR ($\sqrt{Gr} = 3150$), $t/t_0 = 14.14$; (*b*) case HGR ($\sqrt{Gr} = 126\,000$), $t/t_0 = 14.14$; (*c*) case HGR, $t/t_0 = 23.33$.

the forward- and backward-propagating currents is observed starting at the beginning of the slumping phase. This is due to the more rapid growth of the original random disturbances introduced in the lock-gate region. As the currents advance, the billows generated behind the front start losing their predominantly two-dimensional character. After the initial stages of the slumping phase, the billows lose their spanwise coherence over less than $2.5h$ from the front, and only the first two or three billows behind each front are easily identifiable. The interface becomes populated with small three-dimensional eddies. These three-dimensional eddies have enough energy to strongly distort, stretch and eventually break the interfacial billows into smaller turbulent eddies a short time after their formation. The numerical simulation results show that even the billows present just behind the front are strongly disturbed in the spanwise direction. This is due, in part, to their interaction with the lobes and the clefts in the front region.

The shedding of the KH billows introduces an important amount of energy into the interface region, between the two fronts, in the higher-Grashof-number simulation. This energy is redistributed once the billows lose their coherence. Wisps of heavy or light fluid are displaced by the highly energetic three-dimensional structures that resulted from the breaking of the billows. These structures can engulf patches of fluid and transport them away from the interface. Then, by the action of the small-scale eddies and dissipation, these wisps are mixed with the surrounding fluid. Once the current head has passed a certain location, there is no source of energy towards the large scales around that location. Eventually, the large scales present mostly at the interface between the two fluids will be depleted of energy away from the two fronts. As a result, a stably stratified, slightly tilted layer can be observed away from the two fronts in the spanwise-averaged concentration contours past the initial stages of the slumping phase ($t > 18t_0$ for the HGR simulation at $\sqrt{Gr} = 126\,000$). The thickness of this layer in the central part of the channel is nearly constant. Its length grows from about $8h$ at $t = 19t_0$ to about $11h$ at $t = 23.33t_0$ (figure 3*c*). Over this interval, the tilting angle relative to the horizontal is about 14° and is slowly decaying with time. The tilt is due to the fact that the thickness of the layer of unmixed fluid is significantly reduced in the dissipative wake region of each current compared to the region situated around the lock-gate position. This reduction in the thickness is

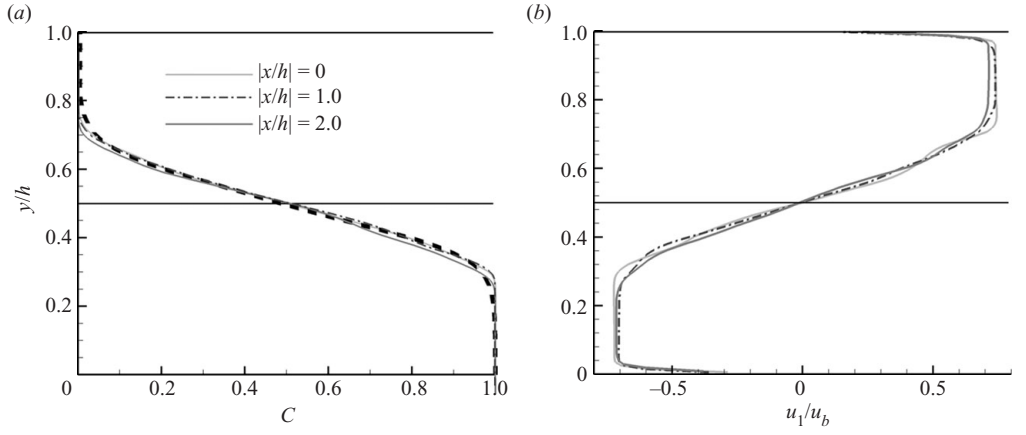

FIGURE 4. Analysis of structure of the lock-exchange flow in the HGR ($\sqrt{Gr} = 126\,000$) simulation in the region in which the stably stratified tilted layer is present. (*a*) Vertical spanwise- and time-averaged concentration profiles at sections $|x/h| = 0.0$, 1.0 and 2.0 with a best fit hyperbolic tangent profile (dashed line). The profiles are shifted in the vertical direction such that $C = 0.5$ occurs at $y/h = 0.5$. (*b*) Vertical spanwise-averaged streamwise velocity profiles, u_1/u_b, at $|x/h| = 0.0$, 1.0 and 2.0, $t/t_0 = 23.33$.

explained by the fact that the coherence of the billows is high, and the interfacial mixing is strongly enhanced inside the dissipative wake region.

More details on the concentration and streamwise velocity distributions within this layer are given in figure 4. The spanwise and time-averaged concentration profiles across the mixing layer are plotted in figure 4(*a*) at $|x/h| = 0$, 1 and 2. These profiles were time averaged between the time the mixing layer forms at a $|x/h| =$ constant location and the time the currents start interacting with the endwalls. The time at which the collapse begins increases with the distance from the position of the lock gate. For example at $|x/h| = 1$ the profiles start collapsing for $t > 20.5t_0$. The concentration profile is still symmetric around $C = 0.5$ at sections with $|x/h| > 0$ but, due to the tilting of the mixing layer, the value of y/h corresponding to $C = 0.5$ is not equal to 0.5 in these sections. Simulation results show that if the mean profiles at different sections are superimposed on top of each other such that $C = 0.5$ occurs at the same point ($y/h = 0.5$ in figure 4*a*), the concentration profiles collapse into one curve that can be approximated using a hyperbolic tangent function. The vertical spanwise-averaged profiles of the streamwise velocity, u_1/u_b, at sections cutting through the mixing layer (figure 4*b*) are also close. Observe the presence of a region of constant streamwise velocity starting at the edge of the boundary layers on the top and bottom walls. The velocity variation in the central part of the channel is close to linear.

3.2. *Energy budget and dissipation rate*

Gravity currents are flows driven by the conversion of potential energy into kinetic energy, with a small part of the energy being dissipated by viscous friction. The local dissipation rate ε_r integrated over the computational domain Ω at a certain moment in time is denoted ε. For LESs, in which the model can directly calculate only the gradients in the resolved velocity field, the total dissipation rate has two components. One is the viscous dissipation ε_0, and the other is the SGS dissipation ε_t, due to

velocity gradients at the unresolved scales:

$$\left.\begin{aligned}
\varepsilon &= \int_0^{L_1}\int_0^{L_2}\int_0^{L_3} \varepsilon_r(x_1, x_2, x_3, t)\mathrm{d}V = \int_\Omega \varepsilon_r \mathrm{d}V = \varepsilon_0 + \varepsilon_t, \\
\varepsilon_0 &= \int_\Omega u_i \frac{\partial}{\partial x_k}\left[\left(\frac{1}{\sqrt{Gr}}\right)\left(\frac{\partial u_i}{\partial x_k} + \frac{\partial u_k}{\partial x_i}\right)\right]\mathrm{d}V, \\
\varepsilon_t &= \int_\Omega u_i \frac{\partial}{\partial x_k}\left[(\nu_{SGS})\left(\frac{\partial u_i}{\partial x_k} + \frac{\partial u_k}{\partial x_i}\right)\right]\mathrm{d}V.
\end{aligned}\right\} \tag{4}$$

The total potential energy over the flow domain is

$$E_p(t) = \int_\Omega C x_2 \mathrm{d}V. \tag{5}$$

The total kinetic energy over the flow domain is

$$E_k(t) = \int_\Omega 0.5 u_i u_i \mathrm{d}V. \tag{6}$$

Following Necker *et al.* (2005), in the case of compositional currents a differential equation relating the rates of change of the potential and kinetic energies can be obtained if the velocity components are assumed to be equal to zero on all the non-periodic boundaries and if the effects of diffusion in the transport equation for the concentration are neglected. The equation is

$$\frac{\mathrm{d}E_k}{\mathrm{d}t} = -\frac{\mathrm{d}E_p}{\mathrm{d}t} - \varepsilon. \tag{7}$$

Integrating (7) with respect to time gives an integral balance equation for the energy:

$$E_k + E_p + E_d = \text{constant} = E_{p0}, \tag{8}$$

where E_{p0} is the total initial potential energy. The term E_d represents the time integral of ε:

$$E_d(t) = \int_0^t \varepsilon(\tau)\,\mathrm{d}\tau. \tag{9}$$

The temporal evolution of the terms in (7) is plotted in figure 5. After the initial acceleration phase, $\mathrm{d}E_k/\mathrm{d}t$ decays in a non-monotonic fashion in both simulations. In the lower-Grashof-number simulation, ε_t is practically negligible over the entire simulated period. In the higher-Grashof-number simulation, the magnitudes of ε and ε_t peak around $t = 10.5t_0$ ($x_f/h \cong 5$). At this stage, the ratio $\varepsilon_t/\varepsilon$ attains its maximum value at 0.67.

For $t > 18t_0$, $\mathrm{d}E_p/\mathrm{d}t$, $\mathrm{d}E_k/\mathrm{d}t$, the total dissipation rate ε and its SGS component ε_t become nearly constant in the higher-Grashof-number simulation. During this equilibrium regime, the ratio of ε to $\mathrm{d}E_p/\mathrm{d}t$ is close to 0.28, and that of $\mathrm{d}E_p/\mathrm{d}t$ to $-\mathrm{d}E_k/\mathrm{d}t$ is 0.72. About 73 % of the total dissipation rate occurs over a distance of $5h$ behind the two fronts (see the discussion of figure 6). Over this region, high values of the local dissipation rate are observed in the mixing layer behind the front, where the billows loose their coherence, and, to a smaller degree, in the near-bed region. Such a regime is expected to be present for currents with $\sqrt{Gr} > 30\,000$, provided the lock

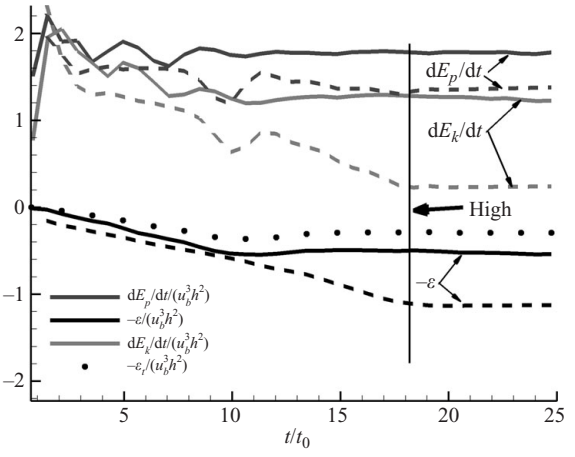

FIGURE 5. Temporal evolution of the terms in the differential equation (7) for the HGR ($\sqrt{Gr} = 126\,000$) three-dimensional simulation (solid lines) and LGR ($\sqrt{Gr} = 3150$) three-dimensional simulation (dashed lines). The SGS part of the total dissipation rate for the HGR simulation is shown using circles. The vertical line marked 'high' corresponds to the start of the regime in which the terms in (7) become close to constant in the HGR simulation.

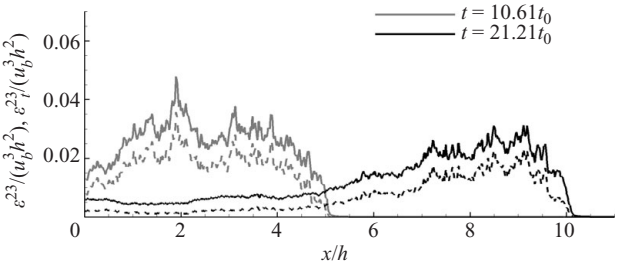

FIGURE 6. Streamwise distribution of $\varepsilon^{23}(x_1)$ (solid lines) and its SGS part $\varepsilon_t^{23}(x_1)$ (dashed lines) at $t/t_0 = 10.61$ and 21.21 in the HGR ($\sqrt{Gr} = 126\,000$) three-dimensional simulation. Their expressions in (10) and (11) were non-dimensionalized by $u_b^3h^2$.

length is sufficient, such that the current will not interact with the endwalls well after $t = 18t_0$. The non-dimensional time needed for this regime to be reached is expected to decrease with the Grashof number, as the three-dimensional turbulence becomes more effective in breaking the coherence of the interfacial vortices.

Information on the spatial and temporal distribution of the dissipation rate within a gravity current is important not only for understanding the physics of lock-exchange flows (e.g. what are the main flow structures responsible for most of the dissipative losses) at different stages of the evolution of the current but also for developing theoretical models of these flows (e.g. see Huppert & Simpson 1980), which incorporate the effect of the dissipation, and determining the parameters in these models. As the dissipation cannot be estimated directly in these simplified models, one possible solution is to calibrate these parameters using the distributions of the dissipation rate determined from numerical simulations. Moreover, the separate contributions of the head and tail regions of the current, or the contribution of the interface region to the total dissipation, can be calculated and modelled independently. In the

following, we concentrate on the analysis of the higher-Grashof-number simulation ($\sqrt{Gr} = 126\,000$).

To study the distribution of the dissipative losses along the channel, the local dissipation rate $\varepsilon_r = \varepsilon_r(x_1, x_2, x_3)$ is integrated over the spanwise and vertical directions. This leads to a variable ε^{23} which is a function only of the streamwise position along the heavier or lighter currents:

$$\varepsilon^{23}(x_1) = -\int^{L_3}\int^{L_2} u_i \frac{\partial}{\partial x_k}\left[\left(\frac{1}{\sqrt{Gr}} + \nu_{SGS}\right)\left(\frac{\partial u_i}{\partial x_k} + \frac{\partial u_k}{\partial x_i}\right)\right] \mathrm{d}x_3 \mathrm{d}x_2. \tag{10}$$

Similarly, the SGS contribution can be calculated as

$$\varepsilon_t^{23}(x_1) = -\int^{L_3}\int^{L_2} u_i \frac{\partial}{\partial x_k}\left[\nu_{SGS}\left(\frac{\partial u_i}{\partial x_k} + \frac{\partial u_k}{\partial x_i}\right)\right] \mathrm{d}x_3 \mathrm{d}x_2. \tag{11}$$

In figure 6 the two distributions of ε^{23} and ε_t^{23} are plotted at two non-dimensional times ($t/t_0 = 10.61$ and 21.21) which are representative of the evolution of the heavier current over the slumping phase before and after the formation of the stably stratified tilted layer. Consistent with the variation of the total dissipation rate $\varepsilon = \int^{L1} \varepsilon^{23}(x_1)\mathrm{d}x_1$ in figure 5, the area beneath the curve defined by the variation of ε^{23} with x peaks at $t \cong 10.5t_0$. At this moment, large dissipative losses are observed over virtually the entire length of the heavier current.

As previously discussed, a mixing layer of nearly constant width, in which large-scale structures are not observed, starts developing as the currents advances. For $18t_0 < t < 25t_0$, the distance between the front and the extremity of the mixing layer region that does not contain large-scale structures is nearly constant ($\cong 5h$). For example at $t = 21.21t_0$ (see figure 6) the extremity of this region is situated at $x/h \cong 5$, and the front is situated at $x/h = 10$. The values of ε^{23} are significantly smaller in the region with $x/h < 5$ compared to the ones between $x/h = 5$ and the front. The flow inside the current is strongly turbulent and contains large-scale structures over a distance of $5h$ from the front. The dissipation rate over this region represents 73 % of the dissipation rate occurring in the $x/h > 0$ region at $t = 21.21t_0$. This percentage is nearly constant once the current reaches the regime in which the terms in the energy equation (7) are constant in time ($t > 18t_0$).

The simulations showed that the presence of a highly turbulent flow behind the front of gravity currents with $R \ll 1$ induces the formation of a stably stratified interface layer, depleted of large scales, in the later stages of the slumping phase. At about the same time, the rate of change of the kinetic and potential energies and the total dissipation rate become independent of time. These flow features are not observed for gravity currents with $R \ll 1$ at $\sqrt{Gr} < 10^4$. In the next section, we study the evolution, structure and energy budget of gravity currents with $R = O(1)$.

4. Gravity currents with a small volume of release ($R = O(1)$)

A main goal of this section focusing on the evolution of currents with $R = O(1)$ during and past the transition to the buoyancy–inertia phase is to understand to what degree the dynamics of full-depth lock-release flows and their energy budget are affected by the Grashof number for $10^4 < \sqrt{Gr} < 10^6$. This is an important question, as at $\sqrt{Gr} \cong 10^6$ the gravity current is much closer to the conditions encountered in most geoscience applications, while most of the presently available information on these flows come from studies conducted at much lower Grashof numbers.

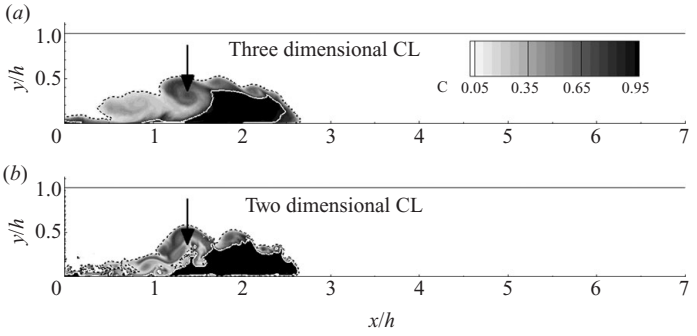

FIGURE 7. Concentration contours showing the structure of the gravity current at $t/t_0 = 4.6$. (a) Spanwise-averaged contours, case CL ($R = 1.78$, $\sqrt{Gr} = 47\,750$), three-dimensional simulation; (b) Case CL, two-dimensional simulation. Position of the bore is indicated by an arrow. The solid and dashed lines correspond to the $C = 0.9$ and $C = 0.1$ concentration levels, respectively.

4.1. *Role of the Grashof number*

Among cases A ($R = 0.67$), B ($R = 1$) and CL ($R = 1.78$), the distance at which the bore overtakes the front is the shortest for case CL ($x/h = 5.5$; table 2). Thus, in the following discussion we focus on case CL to study the evolution of the current during the transition to the buoyancy–inertia phase and its initial stages. Comparison between cases CL ($R = 1.78$, $\sqrt{Gr} = 47\,750$) and CH ($R = 1.78$, $\sqrt{Gr} = 10^6$) allows the study of Grashof number effects on the evolution of lock-release currents for which the flow behind the front is strongly turbulent The experiments of Hacker *et al.* (1996) did not report visualizations of the current after the end of the transition to the buoyancy–inertia phase.

Figures 7(a) and 8(a) visualize the structure of the current during the transition to the buoyancy–inertia phase for case CL (three-dimensional results). While during the initial stages of the transition to the inertia–buoyancy phase (e.g. see figure 7a) the interfacial billows behind the head are strongly coherent, during the later stages of the transition (e.g. see figure 8a), when the bore is situated at less than $0.5h$ from the front, a mildly stratified tail region develops in the three-dimensional simulation, similar to the experiment (see figure 8b). The three-dimensional simulation also successfully captures the dimension of the region containing unmixed lock fluid behind the front and the overall shape of the current. Simulation results also show that starting with the initial stages of the buoyancy–inertia phase, the flow at the front starts mixing in the three-dimensional simulation, and the front velocity decays with time. The highest concentrations inside the current occur in a small elongated region near the bed, some distance behind the front. The head and the stratified tail of the current maintain their compact shape, and the coherence of the large-scale structures present in the tail decays significantly.

Comparison of figures 7(a) and 7(b) shows that the two-dimensional simulation captures satisfactorily the overall shape of the current and the dimensions of the region containing unmixed fluid behind the front during the initial stages of the transition to the buoyancy–inertia phase. Still, the coherence of the interfacial billows is slightly larger compared to the three-dimensional simulation. In contrast, in the later stages of the transition to the buoyancy–inertia phase the mildly stratified tail region observed in the experiment (figure 8b) and three-dimensional simulation

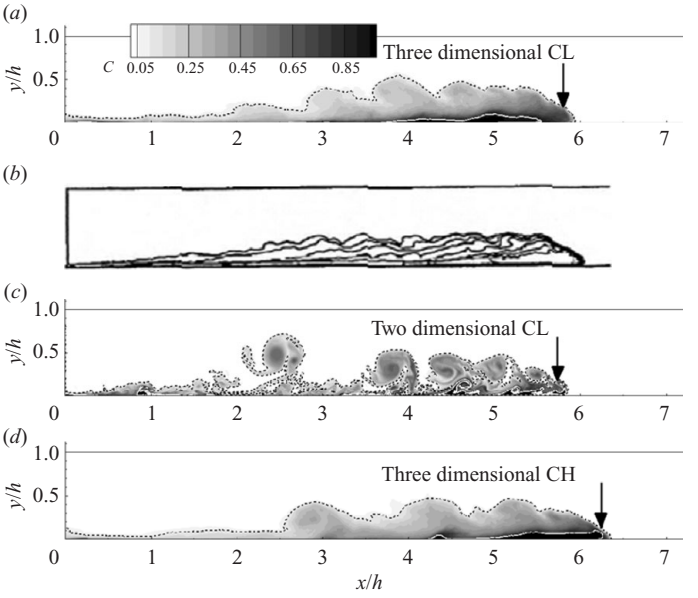

FIGURE 8. Concentration contours showing the structure of the gravity current at $t/t_0 = 12.4$. (*a*) Spanwise-averaged contours, case CL ($R = 1.78$, $\sqrt{Gr} = 47\,750$), three-dimensional simulation; (*b*) experimental results of Hacker *et al.* (1996) for case CL; (*c*) case CL, two-dimensional simulation; (*d*) spanwise-averaged contours, case CH ($R = 1.78$, $\sqrt{Gr} = 10^6$), three-dimensional simulation. Position of the bore is indicated by an arrow. The solid and dashed lines correspond to the $C = 0.9$ and $C = 0.1$ concentration levels, respectively. Reproduced with permission from Hacker, J., Linden, P. F. & Dalziel, S. B. 1996 Mixing in lock-release gravity currents. *Dyn. Atmos. Oceans* **24**, 183–195.

(figure 8*a*) is absent in the two-dimensional simulation (figure 8*c*). The interfacial vortices maintain their coherence, and the compact head region is virtually absent in the two-dimensional simulation. Several other numerical studies (e.g. Cantero *et al.* 2007; Hallez & Magnaudet 2008) observed the increased coherence of the interfacial vortices in two-dimensional simulations. The increases coherence is due to the absence of the three-dimensional breakup mechanism. Comparison of the simulations shows the disagreement between the three-dimensional and two-dimensional predictions continues to grow during the buoyancy–inertia phase. Consistent with the results of Cantero *et al.* (2007), two-dimensional simulations significantly underpredict the speed of the front during the buoyancy–inertia phase.

Qualitatively, the evolution of the heavier current in case CH is similar to case CL during the transition to the buoyancy–inertia phase (e.g. compare figure 8*a* to figure 8*d*). The region containing lock fluid extends closer to the front in case CH. The front travels a slightly longer distance in the CH simulation, such that when the bore overtakes the front the difference is close to $0.4h$. The difference between the positions of the two fronts grows at a faster rate during the buoyancy–inertia phase. For instance, the difference is about $1h$ at $t/t_0 = 25$. Thus, Grashof number effects on the development of flow instabilities and current evolution are small over the range $4 \times 10^4 < \sqrt{Gr} < 10^6$.

Figure 9 visualizes the interface between the gravity current and the ambient fluid for case CL using a concentration isosurface ($C = 0.5$) at $t = 16t_0$ during the buoyancy–inertia phase. Though the interfacial billows in the dissipative wake

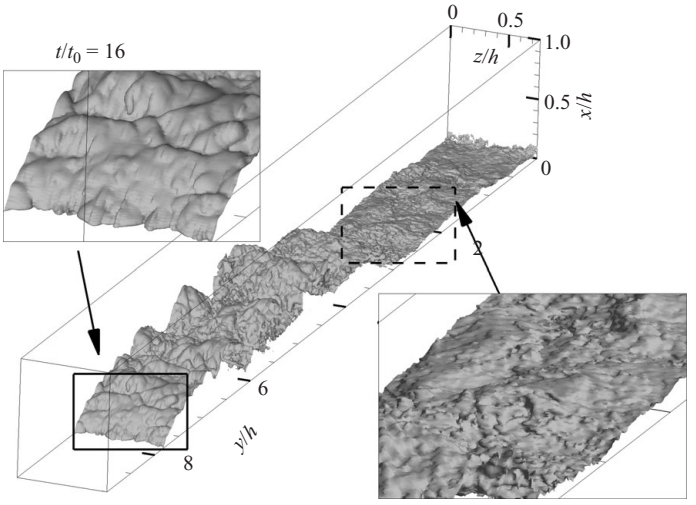

FIGURE 9. Visualization of the current interface at $t/t_0 = 16.0$ using a concentration isosurface ($C = 0.5$) in the three-dimensional simulation of case CL ($R = 1.78$, $\sqrt{Gr} = 47\,750$) with insets showing development of the lobe and cleft structures at the front and decay of turbulence in the tail.

region are strongly deformed in the spanwise direction, they extend over the entire width of the computational domain. This suggests the formation of these structures remains a predominantly two-dimensional process even for $\sqrt{Gr} > 10^4$. The spanwise deformation of the billows starts in the formation region and is due to the lobes and clefts at the front (see inset in figure 9). Similar to the HGR simulation ($\sqrt{Gr} = 126\,000$) with $R \ll 1$, interactions between the billows and the front structures are observed. Simulation results also show that as the current transitions to the buoyancy–inertia phase, the intensity of these interactions increases.

During the buoyancy–inertia phase the flow remains strongly turbulent behind the head region for a distance that includes part of the tail. As one moves away from the head region, the coherence of the large-scale coherent structures is practically lost. For example at $t = 16t_0$ the region with $x < 6h$ is populated with small-scale energetic eddies that produce a relatively mildly stratified region behind the head of the current. Eventually, these small-scale eddies, which lose their energy by mixing the lock and ambient fluid, dissipate, and the flow starts to relaminarize.

Figure 10(a) shows the structure of the gravity current in case D ($R = 1$, $\sqrt{Gr} = 530$) at $t = 15t_0$ before the bore catches the front. The size of the bulk-shaped head shrinks in time as the bore advances. Compared to the higher-Grashof-number cases ($\sqrt{Gr} > 10^4$), very little mixing is taking place between the lock fluid and the ambient fluid. No interfacial billows are shed behind the front because the viscosity is too high to allow the KH instabilities to grow. The current advances over a layer of light fluid that is much thicker ($0.1h$–$0.13h$) than that observed in the simulations for which $\sqrt{Gr} > 10^4$. Eventually, the size of the head diminishes to the point at which the bulk-shaped head disappears (figure 10b). This corresponds to the transition from the slumping phase to the viscous–buoyancy phase (see the discussion of figure 14). The inset in figure 10(b) compares the predicted shape of the current with the analytical solution derived by Huppert (1982) for the viscous–buoyancy regime. Good agreement is observed over the downstream part of the current.

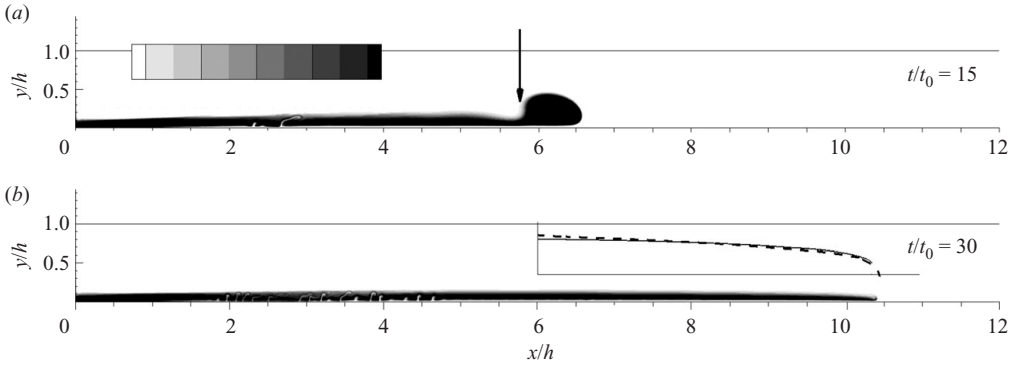

FIGURE 10. Concentration contours showing temporal evolution of gravity current for case D ($R = 1.0$, $\sqrt{Gr} = 530$): (*a*) $t/t_0 = 15.0$; (*b*) $t/t_0 = 30.0$. The arrow in (*a*) marks the position of the bore. The inset in (*b*) shows the comparison of the computed shape of the gravity current during the viscous–buoyancy phase (solid line) with the analytical solution (dashed line) obtained by Huppert (1982) for the viscous–buoyancy regime. The aspect ratio is 1:4 in the x–y plot that shows the comparison with the analytical solution.

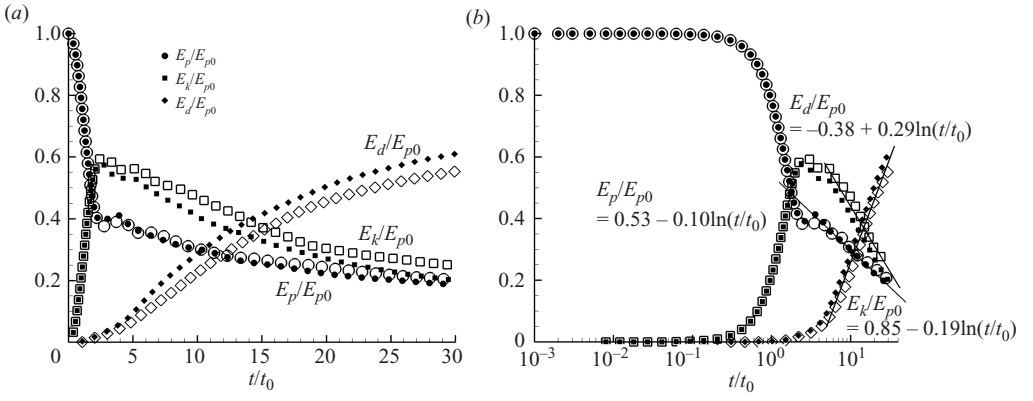

FIGURE 11. Time history of the potential energy E_p (circles), kinetic energy E_k (squares) and integral of the total dissipation E_d (diamond) in the CL ($R = 1.78$, $\sqrt{Gr} = 47\,750$) three-dimensional simulation (filled symbols) and the CH ($R = 1.78$, $\sqrt{Gr} = 10^6$) three-dimensional simulation (open symbols). (*a*) Linear–linear scale; (*b*) linear–log scale.

4.2. *Energy budget and dissipation rate*

The variations in time of E_k, E_p and E_d for cases CL ($R = 1.78$, $\sqrt{Gr} = 47\,750$) and CH ($R = 1.78$, $\sqrt{Gr} = 10^6$) are shown in figure 11. These variables are non-dimensionalized with the initial value of the total (potential) energy, E_{p0}. As observed from figure 11(*a*) the maximum value of E_k is obtained around the time the bore has formed ($t/t_0 \cong 2.5$). By that time, about 59 % of the initial potential energy has been converted into kinetic energy and the dissipative losses are very small ($\cong 2\,\%$) for cases CL and CH. Results for cases A and B are similar. Most of the differences between the energy balance in the CL and CH simulations occur between the time the bore has formed and the time the bore catches the front. The increase in E_d is larger in case CL, and conversely, the decay of E_k is smaller, such that when the bore catches the front ($t = 10$–$11t_0$), the difference between E_k and E_d is about 7 %

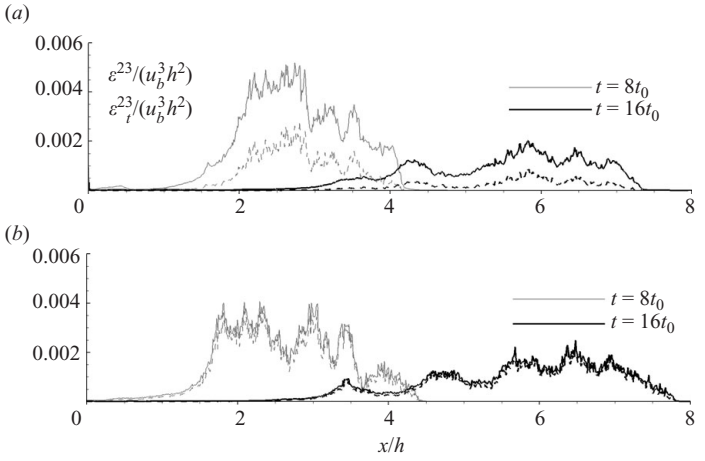

FIGURE 12. Streamwise distribution of $\varepsilon^{23}(x_1)$ (solid line) and its subgrid stress part $\varepsilon_t^{23}(x_1)$ (dashed line) at $t/t_0 = 8$ and 16. (*a*) Case CL ($R = 1.78$, $\sqrt{Gr} = 47\,750$), three-dimensional simulation; (*b*) case CH ($R = 1.78$, $\sqrt{Gr} = 10^6$), three-dimensional simulation.

of the total initial energy. Meanwhile, the variation of E_p until the bore catches the front is very similar in both simulations. The relative variations of E_p, E_k and E_d are essentially independent of the Grashof number once the current is in the buoyancy–inertia phase (see figure 11*a* for $t > 11t_0$). The values of E_d and E_k over the buoyancy–inertia phase in the CL simulation (figure 11*a*) are consistently 6–8 % higher and, respectively, smaller compared to those observed in the CH simulation. Grashof number effects on E_p continue to be insignificant. Past the later stages of the transition to the buoyancy–inertia phase, after the kinetic energy starts decaying due to the strong increase in the dissipative losses, the variations of E_p, E_k and E_d become logarithmic (figure 11*b*):

$$\left.\begin{aligned} E_p/E_{p0} &= 0.53 - 0.10\ \ln\,(t/t_0),\\ E_k/E_{p0} &= 0.5 - 0.19\ \ln\,(t/t_0),\\ E_d/E_{p0} &= -0.38 + 0.29\ \ln\,(t/t_0). \end{aligned}\right\} \tag{12}$$

The streamwise distributions of ε^{23} and ε_t^{23} in figure 12 reveal the regions in which most of the dissipative losses occur at the different stages of the current evolution. Between the time when the bore forms and the time when the bore overtakes the front, the dissipation in the tail region (e.g. $x/h < 2.9$ at $t = 8t_0$) is larger in case CL. The difference in E_d between the CL and CH simulations (figure 11*a*) is due primarily ($> 80\,\%$) to the larger dissipation taking place over the tail region in case CL. Over this time interval Grashof number effects are quantitatively significant.

After the bore overtakes the front (e.g. see distributions at $t/t_0 = 16$ in figure 12), the variations of ε^{23} over the head and tail regions in the CL and CH simulations are very similar and Grashof number effects are not significant. Though the streamwise distributions of ε^{23} are very close, the contribution of the SGS component is quite different in the two simulations. For example in the CH simulation at $t = 16t_0$, the SGS component accounts for more than 80 % of the total dissipation over nearly the entire length of the current. In the CL simulation, the SGS component accounts for less than 25 % of the total dissipation. Observe also that the total and the SGS dissipation rates become very small close to the endwall in the two simulations (e.g.

for $0 < x/h < 3$ at $t/t_0 = 16$). This means the flow relaminarizes in that region, which is consistent with the results in figure 9.

Models that try to predict the propagation of internal bores generally assume that most of the energy loss occurs in either the upper or the lower layer. Recent models (e.g. Klemp, Rotunno & Skamarock 1997) assume the energy loss occurs in the upper layer, as proposed by Benjamin (1968) for gravity currents, and the energy is conserved in the lower layer. However, there is no formal proof that this hypothesis is correct. The instantaneous distributions of the spanwise-averaged dissipation rate after the bore has formed support this hypothesis. For low-Grashof-number currents (case D) in which no interfacial billows are shed behind the head and the thickness of the lower layer is clearly defined, most of the dissipation behind the bore occurs in the upper layer. For example at $t/t_0 = 15$ (figure 10*a*) results show that 68 % of the total dissipation rate occurs inside the head, 28 % in the upper layer behind the bore and only 4 % in the lower layer. This also appears to be the case for higher-Grashof-number currents, though in this case it is more difficult to distinguish between the dissipation associated with the interfacial billows and the one induced by the bore passage.

4.3. *Front velocity*

The bore position and velocity are difficult to estimate directly from the concentration contour plots because the bore propagates into the stratified layer of fluid that corresponds to the body of the current. A more accurate way to determine the bore position is to plot the temporal evolution of the concentration on a line situated at a small distance ($y/h = 0.1$) from the bottom. The $C(x, t)$ plots are shown in figure 13 for case CL. A dark region in the form of a triangle is observed. The two lines that intersect at a small angle in figure 13 correspond to the front and bore trajectories. The slope of the lower line, which makes a smaller angle with the time axis, corresponds to the speed of the front, while the slope of the top line corresponds to the speed of the reflected bore. The top line cuts through an array of dark streaks. These streaks correspond to the passage of the interfacial billows over the $y/h = 0.1$ line. As the speed and bore trajectories are close to straight lines, the front and bore velocities are nearly constant until the position and time at which the intersection takes place ($x_f/h = 5.5$, $t = 11.5t_0$ for case CL). The non-dimensional streamwise length at which the bore overtakes the front $l = (x_f - x_0)/x_0$ (x_f is the front position) is close to 8.8. Once the bore catches the front, the front trajectory starts curving up, and its slope with the time axis starts decaying. Similar results were obtained from simulations of cases A ($R = 0.67$, $\sqrt{Gr} = 30\,980$), CL ($R = 1.78$, $\sqrt{Gr} = 47\,750$), CH ($R = 1.78$, $\sqrt{Gr} = 10^6$) and D ($R = 1.0$, $\sqrt{Gr} = 530$) in which the domain is long enough, such that the bore catches the front before the current reaches the end boundary. These results are summarized in table 2. They show that for a given value of R, the non-dimensional location at which the bore overtakes the front is not sensitive to the value of the Grashof number for strongly turbulent currents (e.g. compare values for cases CL and CH).

The front velocity before the bore overtakes the front expressed as a Froude number $Fr_f = U_f/u_b$, and the values of the bore velocity U_{bore}/u_b are 0.45 and 0.62 for case CL. The corresponding values for case CH are 0.485 and 0.65. The results for the other simulations are summarized in tables 2 and 3. Though the increase of the Grashof number between cases CL and CH produced a 6–7 % increase in the front and bore velocities, their ratio remained close to constant at 1.35. The present study shows the ratio changes only by 2 % for $10^2 < \sqrt{Gr} < 10^6$. Case CH ($Re_f = 248\,000$)

Case	$U_{bore}/\sqrt{g'h}$	$U_f/\sqrt{g'h}$	U_{bore}/U_f
A	0.60	0.44	1.36
B	0.61	0.45	1.35
CL	0.62	0.45	1.35
CH	0.65	0.485	1.35
D	0.49	0.37	1.33

TABLE 3. Comparison of bore and front velocities.

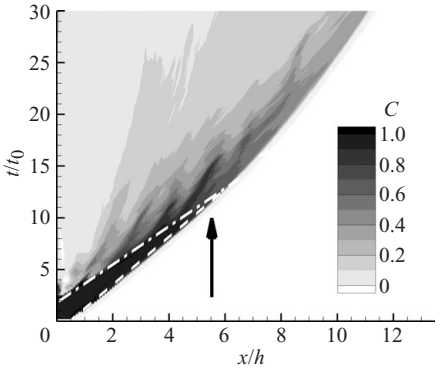

FIGURE 13. Evolution of concentration with time along the x-axis for case CL ($R = 1.78$, $\sqrt{Gr} = 47\,750$). Distance from the bottom wall is $y/h = 0.1$. The dashed line corresponds to the front trajectory until the bore overtakes the front. The dashed–dotted line corresponds to the bore trajectory. The arrow marks the location at which the bore overtakes the front.

has $Fr_f = 0.485$, which is close to the theoretical value of 0.5 obtained by Benjamin (1968) for an energy-conserving current. Keulegan (1958) found $Fr_f = 0.48$ at front Reynolds numbers around 150 000.

Figure 14 shows the temporal evolution of the front position in log–log scale for several cases with $R = O(1)$. Following the initial short acceleration phase, a region in which the slope is approximately constant and equal to one (this corresponds to $x_f \sim t$ or $U_f = \text{constant}$) is present in all the cases. The bore forms at $t/t_0 = 2.5$. For cases CL and CH, there is a change in the slope of the front trajectory between $t = 10$–$11.5t_0$ (bore overtakes the front) and $t = 20t_0$. The change in the slope corresponds to a decay of the front velocity. For $t > 20t_0$, the slope in the log–log plot becomes nearly constant and equal to approximately 0.63 in case CL and to 0.65 in case CH. This slope is equal to the exponent β in the power law decay $x_f \sim t^{\beta}(U_f \sim t^{\beta-1} = t^{-\alpha})$. The values of α and β in case CH are very close to the theoretical values of $1/3$ and $2/3$ (Fannelop & Waldman 1972; Hoult 1972) corresponding to the buoyancy–inertia phase. In case B ($R = 1$, $L_1/h = 9$) the flow conditions are such that the current reaches the end boundary before the end of the transition to the buoyancy–inertia phase; so the change in the slope towards the $2/3$ value is not complete. For case D, the change in the slope takes place more abruptly. Similar to cases CL and CH, the front trajectory reaches a constant slope after the bore overtakes the front. This slope is equal to $1/5$ ($U_f \sim t^{-4/5}$), which is the expected value for the variation of the front position with time during the viscous–buoyancy phase (Rottman & Simpson 1983).

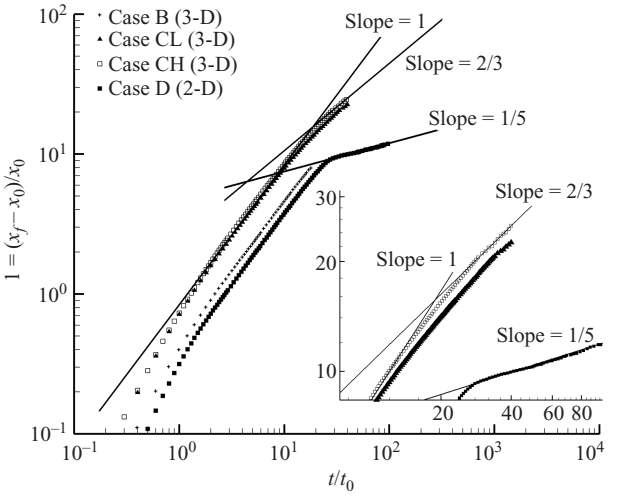

FIGURE 14. Evolution of the non-dimensional front position l with time in log–log scale for cases B ($R = 1.0$, $\sqrt{Gr} = 87\,750$), CL ($R = 1.78$, $\sqrt{Gr} = 47\,750$), CH ($R = 1.78$, $\sqrt{Gr} = 10^6$) and D ($R = 1.0$, $\sqrt{Gr} = 530$). The inset shows an enlarged view of the $l = l(t/t_0)$ curves in the later stages of the evolution of the gravity current.

The present results demonstrated that a change in the Grashof number between $\sqrt{Gr} \cong 3 \times 10^4$ and $\sqrt{Gr} = 10^6$ did not result in significant qualitative changes in the structure and evolution of a gravity current with $R = O(1)$. The temporal variations of the kinetic and potential energies were logarithmic past the later stages of the transition to the buoyancy–inertia phase. Quantitatively, the behaviour of the gravity current with $\sqrt{Gr} = 10^6$ was closer to that expected for inviscid currents. In the next section, we analyse the near-wall flow structure of high-Grashof-number currents. The focus is on gravity currents with $R = O(1)$ and $\sqrt{Gr} > 3 \times 10^4$.

5. Near-wall flow structure and bed friction velocity

Knowledge of the spatial and temporal distributions of the bed friction velocity is necessary to estimate global quantities related to the capacity of the current to entrain bed particles (e.g. the total amount of sediment entrained by the current and the associated bed morphology changes), especially in numerical models in which the entrainment is a function of the difference between the actual bed shear stress and the critical bed shear stress value given by Shields's diagram. Two main questions we investigate are (i) how do the bed friction velocity distributions change with time during and past the transition to the buoyancy–inertia phase for currents with $R = O(1)$, and (ii) how are these distributions, and thus the capacity of the current to entrain sediment, affected by the Grashof number? No such information is yet available for high-Grashof-number currents.

In all the simulations with $R = O(1)$ and $\sqrt{Gr} > 3 \times 10^4$, a region containing streaks of high and low streamwise velocities forms during the slumping phase. Such a region is also present in case HGR ($\sqrt{Gr} = 126\,000$) for which $R \ll 1$. The length of this region increases until the bore overtakes the front. Then, the length of the streaky region remains approximately constant. After some time (e.g $25t_0$ for case CL) the length of the streaky region starts decaying. At a certain point, as the fluid at the front continues to decelerate and the height of the current to decrease, the strength

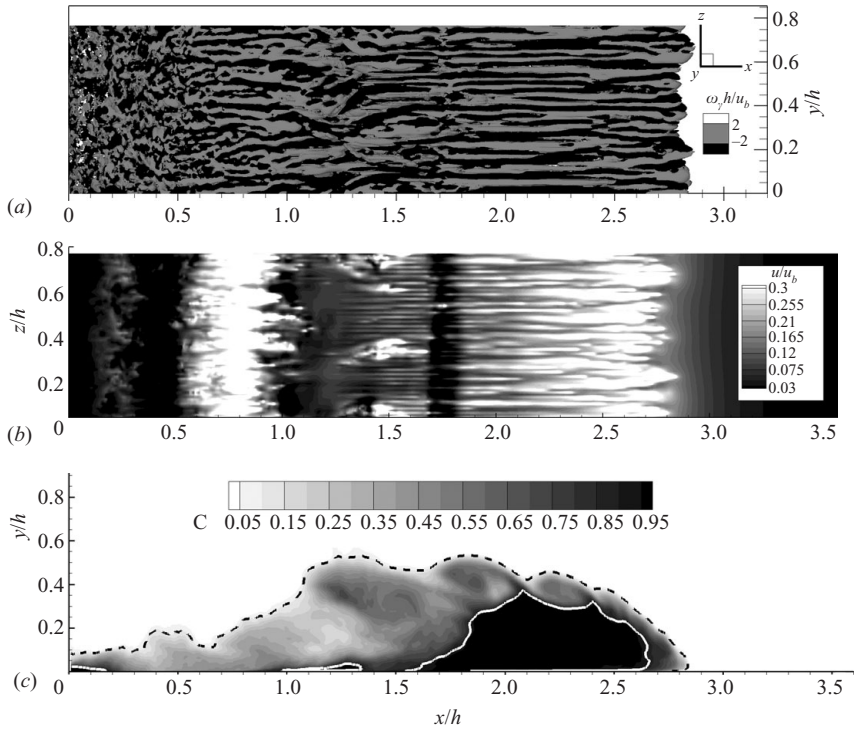

FIGURE 15. Visualization of the flow structure in the near-wall region at $t/t_0 = 5$ for case B ($R = 1.0$, $\sqrt{Gr} = 87\,750$). (*a*) Vertical vorticity contours on the bottom wall; (*b*) streamwise velocity contours showing the high and low streaks of streamwise velocity in a plane located at about 11 wall units from the bottom wall; (*c*) spanwise-averaged concentration contours. The light and dark vorticity contours in (*a*) correspond to $\omega_y = 2u_b/h$ and $\omega_y = -2u_b/h$, respectively. The solid and dashed lines in (*c*) correspond to the $C = 0.9$ and $C = 0.1$ concentration levels, respectively.

of the turbulence in the region behind the front decays below levels at which it can sustain the streaks.

The streamwise velocity contours in a horizontal plane situated at about 11 wall units from the bottom wall are plotted in figure 15, along with the vertical vorticity contours on the bottom wall for case B ($R = 1$, $\sqrt{Gr} = 87\,750$) at $t/t_0 = 5$ after the bore has formed. In the cases with $R = O(1)$ the streaky structure observed in the streamwise velocity and vertical vorticity contours is present mainly beneath the head and dissipative wake regions (e.g. for $0.5 < x/h < 2.8$ in figure 15) after the bore forms. Case B ($R = 1$) was used to illustrate this phenomenon because it has the highest Grashof number ($\sqrt{Gr} = 87\,750$) among the well-resolved three-dimensional simulations. The velocity streaks essentially disappear in the tail region because the local turbulent flow is not strong enough for the streaks to form. In fact, behind the region containing unmixed lock fluid ($x < 1.6h$ in figure 15*c*), the variations in the streamwise velocity are mostly associated with the presence of interfacial billows. These billows induce large spanwise bands of low ($x \cong 1.7h$) and high ($x \cong 0.75h$) streamwise velocities. The average width of these streaks is about $0.025h$ (approximately 40 wall units), and their average length decays from about $0.8h$ ($\cong 1200$ wall units) near the front to about $0.5h$ ($\cong 800$ wall units) towards the end of the streaky region. The streaks are larger in terms of wall unit dimensions compared

to the ones observed in fully turbulent boundary layers and channel flows. This is expected, as the flow conditions behind the front of the current at a certain front Reynolds number are not exactly equivalent to those in a fully turbulent channel flow at a channel Reynolds number that is equal to the front Reynolds number. One should also mention that in the HGR simulation ($\sqrt{Gr} = 126\,000$) with $R \ll 1$ the average length of the streaks was close to $0.5h$ during the slumping phase and varied less with the distance from the front.

One limitation of the present study is that the effect of bed particles entrained by the compositional current on the near-bed turbulence and the bed shear stress distribution behind the front is not considered. Still, comparison of the bed shear stress distributions for cases CL ($\sqrt{Gr} = 47\,750$) and CH ($\sqrt{Gr} = 10^6$) allows to understand how these distributions change as the current gets closer to the inviscid limit and the importance of scale effects between Grashof numbers at which most laboratory experiments are conducted and a Grashof number that is comparable to the values encountered in practical applications (e.g. gravity currents forming at the bottom of lakes and oceans). The non-dimensional bed friction velocity distributions (u_τ/u_b, where $u_\tau = \sqrt{\tau_b/\rho}$, with τ_b being the modulus of the bed shear stress) obtained in cases CH and CL are discussed in figure 16. The number of mesh points in the spanwise direction in the CL simulation is sufficient to accurately capture the streamwise velocity streaks. This is not the case in the CH simulation in which one expects the streaks to be thinner than the spanwise grid spacing used in the simulation. The distributions of the spanwise-averaged values of u_τ/u_b at different stages of the evolution of the gravity current are shown in figure 17 for both cases. Even for case CH, in which the streaks are not well resolved, the distributions of the spanwise-averaged values of u_τ/u_b are expected to be reasonably well predicted. This is because the bed friction velocity distributions are determined to a large extent by the large-scale eddies present in the head, dissipative wake and tail regions away from the near-bed layer. Despite the larger velocity gradients at the bed, the values of u_τ/u_b are smaller in the CH simulation. This is in part because u_τ is proportional to the square root of the molecular viscosity; so u_τ scales with $Gr^{-1/4}$. On the other hand, the non-dimensional velocity gradients at the bed are larger in the CH simulation.

Figure 16 compares the distributions of u_τ at $t = 8t_0$, when the bore is at $1.2h$ behind the front. Individual streaks are clearly distinguishable in the CL simulation (figure 16*b*). The positions of the elongated patches of high u_τ values in the front region correlate well with that of the primary and secondary lobes forming at the front. The length of the region containing streaks of high u_τ values behind the front is $1.4h$. The only other region in which the values of u_τ/u_b are amplified in case CL is situated around $x/h = 1.9$, slightly behind a strongly coherent interfacial billow. These values are about 40–50 % lower than the ones induced by the current immediately behind the front (figure 17).

In the CH simulation (figure 16*a*) the region of high u_τ values associated with the presence of the streaks extends over a similar distance behind the front ($1.2h$–$1.4h$). However, the individual bed friction velocity streaks are hardly recognizable, and the local distribution of u_τ is more uniform in the region in which streaks are present. This is expected, as the physical dimensions of the streaks are decaying with the increase in the Grashof number, similar to constant-density turbulent channel flows in which the length and width of the streaks expressed in wall units are expected to be close to constant. The interfacial billows induce several bands of large u_τ/u_b values over a distance of $2.7h$ behind the front. In contrast to case CL, the values inside the

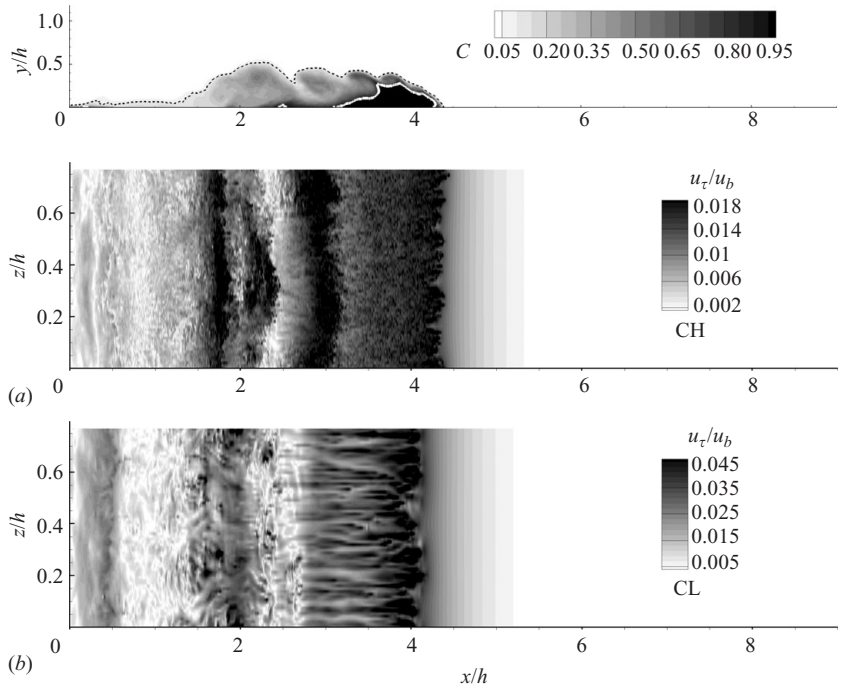

FIGURE 16. Spatial distribution of the friction velocity u_τ/u_b on the bottom wall at $t/t_0 = 8$. (*a*) Case CH ($R = 1.78$, $\sqrt{Gr} = 10^6$), $x_f/h = 4.4$; also shown are the spanwise-averaged concentration contours; (*b*) case CL ($R = 1.78$, $\sqrt{Gr} = 47\,750$), $x_f/h = 4.15$. The solid and dashed lines in the concentration contour plot for case CH correspond to the $C = 0.9$ and $C = 0.1$ concentration levels, respectively.

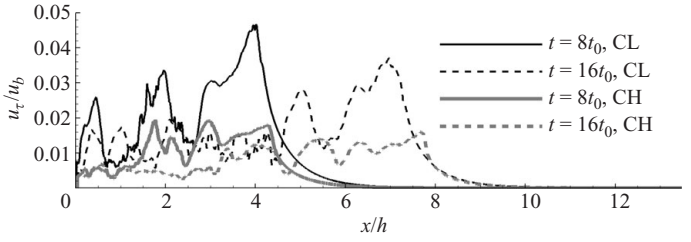

FIGURE 17. Streamwise variation of the spanwise-averaged friction velocity on the bottom wall for case CL ($R = 1.78$, $\sqrt{Gr} = 47\,750$) at $t/t_0 = 8$ (black solid line) and $t/t_0 = 16$ (black dashed line) and case CH ($R = 1.78$, $\sqrt{Gr} = 10^6$) at $t/t_0 = 8$ (grey solid line) and $t/t_0 = 16$ (grey dashed line).

spanwise bands are comparable to the ones observed close to the front (see figure 17). Also, compared to case CL some of the spanwise bands of high u_τ/u_b values no longer extend over the whole width of the domain (e.g. band centred around $x/h = 2.2$), and their axes are more deformed in the spanwise direction.

The distributions of the spanwise-averaged values of u_τ/u_b during the buoyancy–inertia phase are shown in figure 17 at $t = 16t_0$, when the front velocity is less than $0.5U_f$. As a result of the reduction in the front Reynolds number, the turbulence intensity is also decaying behind the front as the current propagates during the buoyancy–inertia phase. This has a larger influence on case CL for which the front

Reynolds number is only 5400 at $t = 16t_0$. As shown in figure 17, in case CL the only regions in which the values of u_τ/u_b are comparable to the largest levels observed before the start of the buoyancy–inertia phase (e.g. at $t = 8t_0$) are situated just behind the front and around $x/h = 4.9$. In case CH, though the levels of u_τ/u_b at $t = 16t_0$ have dropped over most of the length of the current compared to the levels observed at $t = 8t_0$, they remain comparable to the values observed at the front ($u_\tau/u_b \cong 0.014$) over quite a large distance ($\cong 4.5h$) behind the front.

The largest spanwise-averaged values of u_τ/u_b in the CL and CH simulations are close to 0.04 and 0.02, respectively. If one arbitrarily defines a threshold value for sediment entrainment to occur at values larger than half of the maximum value, the total length of the regions that can entrain sediment is higher in the higher-Grashof-number simulation, and the differences increase with time, especially after the start of the buoyancy–inertia phase (e.g. $3h$ in case CH compared to $2.5h$ in case CL at $t = 8t_0$ and $4.3h$ in case CH compared to $2.5h$ in case CL at $t = 16t_0$). Moreover, while in case CH the values of u_τ/u_b over the dissipative wake region and part of the tail remain very close to the ones observed just behind the front, in case CL the values of u_τ/u_b in the same regions are at least 30 % lower than the ones observed close to the front. Thus, higher-Grashof-number gravity currents are more effective in entraining sediment, especially during the buoyancy–inertia phase.

6. Summary and conclusions

In the first part of the paper, results of two three-dimensional LESs were used to study the physics of compositional gravity currents with a large volume of release ($R \ll 1$) during the slumping phase. In the higher-Grashof-number simulation ($\sqrt{Gr} = 126\,000$) the flow behind the front was strongly turbulent. In contrast with the lower-Grashof-number simulation in which the interfacial billows maintained their spanwise coherence over the whole length of the current, in the higher-Grashof-number simulation the interfacial billows were found to lose their spanwise coherence over less than $2.5h$ from the front past the initial stages of the slumping phase. The interface region became populated with small-scale energetic eddies that broke the interfacial two-dimensional billows into smaller structures. As a result, a stably stratified, slightly tilted layer developed in the interface region away from the two fronts starting around $t \cong 18t_0$. This layer does not contain large-scale structures. The concentration profiles across this layer can be approximated by a hyperbolic tangent function. Such a layer is expected to form in cases in which the flow in the region behind the front is highly turbulent. The threshold value in terms of the minimum Grashof number is around $\sqrt{Gr} \cong 35\,000$.

The analysis of the terms in the transport equation for the total kinetic energy demonstrated that in the higher-Grashof-number case with $R \ll 1$ the lock-exchange flow reaches an equilibrium regime in which the rate of change of the kinetic and potential energies and the total dissipation rate are essentially constant in time. The equilibrium regime is expected to be observed in finite-volume lock-exchange flows in which the lock length is large enough, such that the currents will reach the endwalls well after $t = 18t_0$. Once the equilibrium regime is reached ($t \cong 18t_0$), the ratio of ε to $\mathrm{d}E_p/\mathrm{d}t$ is close to 0.28 and that of $\mathrm{d}E_p/\mathrm{d}t$ to $-\mathrm{d}E_k/\mathrm{d}t$ is 0.72. Also, the values of the local dissipation rate integrated over the spanwise and vertical directions (ε^{23}) are significantly larger over a distance of $5h$ behind the two fronts. Over this region, about 73 % of the total dissipation rate takes place.

In the second part of the paper, four three-dimensional LESs of full-depth lock-release flows with initial aspect ratios of the lock fluid between 0.67 and 1.78 were conducted at Grashof numbers ($\sqrt{Gr} = 30\,980$, 87 750, 47 750 and 10^6) for which the flow behind the front is strongly turbulent during the transition to and over part of the buoyancy–inertia phase. In particular, in the simulation for which $\sqrt{Gr} = 10^6$, the gravity current is close to the inviscid state that is often assumed in theoretical models. Comparison of the simulations conducted with $\sqrt{Gr} = 47\,750$ and 10^6 showed that the structure of the two currents and their evolution remains qualitatively similar.

For strongly turbulent gravity currents ($\sqrt{Gr} > 3 \times 10^4$) with $R = O(1)$, the temporal variations of the total kinetic energy and total potential energy and the integral of the total dissipation rate were found to be logarithmic past the later stages of the transition to the buoyancy–inertia phase (e.g. $t > 7t_0$ for currents with $R = 1.78$) The streamwise distribution of the local dissipation rate integrated over $x =$ constant planes showed that Grashof number effects were important between the time the bore formed and the time the bore overtook the front. During this time interval the total dissipation rate in the tail region was found to decrease significantly with the Grashof number.

Present results indicate that the ratio between the bore and front velocity is close to 1.35 for a wide range of Grashof numbers. (The ratio increases only by about 2 % between $\sqrt{Gr} = 530$ and $\sqrt{Gr} = 10^6$.) During the buoyancy–inertia phase, the front velocity was found to vary proportional to $t^{-\alpha}$ (the time t is measured from the release), with the constant α being very close to the theoretical value of 1/3 in the simulation for which $\sqrt{Gr} = 10^6$.

Details of the distribution of the bed friction velocity u_τ were investigated at different stages of the evolution of finite-volume lock-release gravity currents with $R = O(1)$. Scale effects were considered by comparing the distributions of u_τ from two simulations in which the only difference was the value of the Grashof number ($\sqrt{Gr} = 47\,750$ versus $\sqrt{Gr} = 10^6$). In both simulations, a region containing streaks was present behind the front. These streaks were induced by the near-wall streamwise velocity streaks forming in the strongly turbulent region behind the front. The length of the streaky region peaked around the time at which the bore reached the front. It then remained approximately constant during the initial stages of the buoyancy–inertia phase (e.g. until $25t_0$ for $\sqrt{Gr} = 47\,750$). Then, the length of the streaky region started to decay due to the strong reduction in the front velocity and height of the current. The dimensions of the streaks decayed with the increase in the Grashof number. This decay produced a more uniform distribution of u_τ behind the front. The overall size of the regions characterized by non-dimensional values of u_τ/u_b larger than half of the maximum value recorded at a certain time was found to increase with the Grashof number. The increase was especially noticeable during the buoyancy–inertia phase. This means that higher-Grashof-number currents will be more effective in entraining sediment from the bed.

In most cases gravity currents propagate over surfaces containing bed forms and topographic bumps that can significantly modify the front velocity, the spatial and temporal distributions of the bed friction velocity and thus the entrainment capacity of the gravity current. Highly resolved numerical LESs of gravity currents propagating over large-scale roughness elements (e.g. arrays of two-dimensional dunes or ribs) can help in clarifying to what extent the findings obtained from experimental and numerical studies of gravity currents propagating over smooth beds can be extrapolated to the case more relevant for practical applications in which the bed is

rough. The impact between a gravity current and a submarine structure (e.g. oil and gas pipes, submerged dams) that can result in a hazard situation is another example of applications in which LESs are well suited to provide the data (e.g. temporal evolution of the forces on the structure) needed to estimate the hazard risk. The present model is being extended to tackle these problems of significant relevance to river, coastal and ocean engineering.

We would like to thank Professor S. B. Dalziel for giving us permission to include some of his experimental results published in the paper by Hacker *et al.* (1996) for comparison and validation of our method. We gratefully acknowledge the National Center for High Performance Computing (NCHC) in Taiwan, in particular Dr W. H. Tsai, for providing substantial computer time as part of the collaborative program between NCHC and IIHR-Hydroscience and Engineering.

REFERENCES

Benjamin, T. B. 1968 Gravity currents and related phenomena. *J. Fluid Mech.* **31**, 209–248.

Britter, R. E. & Simpson, J. E. 1978 Experiments on the dynamics of a gravity current head. *J. Fluid Mech.* **88**, 223–240.

Cantero, M. I., Lee, J. R., Balachandar, S. & Garcia, M. H. 2007 On the front velocity of gravity currents. *J. Fluid Mech.* **586**, 1–39.

Chang, K. S., Constantinescu, G. & Park, S-O. 2006 Analysis of the flow and mass transfer processes for the incompressible flow past an open cavity with a laminar and a fully turbulent incoming boundary layer. *J. Fluid Mech.* **561**, 113–145.

Chang, K. S., Constantinescu, G. & Park, S-O. 2007 The purging of a neutrally buoyant or a dense miscible contaminant from a rectangular cavity. Part 2. The case of an incoming fully turbulent overflow. *J. Hydraul. Engng* **133** (4), 373–385.

Choi, S-U. & Garcia, M. H. 1995 Modeling of one-dimensional turbidity currents with a dissipative Galerkin finite-element method. *J. Hydraul. Res.* **33** (5), 623–648.

Fanneløp, T. K. 1994 *Fluid Mechanics for Industrial Safety and Environmental Protection.* Elsevier.

Fannelop, T. K. & Waldman, G. D. 1972 Dynamics of oil slicks. *AIAA J.* **10**, 506–510.

Germano, M, Piomelli, U., Moin, P & Cabot, W. H. 1991 A dynamic subgrid-scale eddy viscosity model. *Phys. Fluids* A **3**, 1760–1765.

Hacker, J., Linden, P. F. & Dalziel, S. B. 1996 Mixing in lock-release gravity currents. *Dyn. Atmos. Oceans* **24**, 183–195.

Hallez, Y. & Magnaudet, J. 2008 Effects of channel geometry on buoyancy-driven mixing. *Phys. Fluids* **20**, 053306.

Hallworth, M. A., Huppert, H. E., Phillips, J. C. & Sparks, R. S. J. 1996 Entrainment into two-dimensional and axisymmetric turbulent gravity currents. *J. Fluid Mech.* **308**, 289–311.

Härtel, C., Carlsson, F. & Thunblom, M. 2000*a* Analysis and direct numerical simulation of the flow at a gravity-current head. Part 2. The lobe-and-cleft instability. *J. Fluid Mech.* **418**, 213–229.

Härtel, C., Meiburg, E. & Necker, F. 2000*b* Analysis and direct numerical simulation of the flow at a gravity-current head. Part 1. Flow topology and front speed for slip and no-slip boundaries. *J. Fluid Mech.* **418**, 189–212.

Hoult, D. P. 1972 Oil spreading on the sea. *Annu. Rev. Fluid Mech.* **4**, 341–368.

Huppert, H. 1982 The propagation of two-dimensional and axisymmetric viscous gravity currents over a rigid horizontal surface. *J. Fluid. Mech.* **121**, 43–58.

Huppert, H. & Simpson, J. E. 1980 The slumping of gravity currents. *J. Fluid. Mech.* **99**, 785–799.

Keller, J. J. & Chyou, Y.-P. 1991 On the hydraulic lock-exchange problem. *J. Appl. Math. Phys.* **42**, 874–910.

Keulegan, G. H. 1957 An experimental study of the motion of saline water from locks into fresh water channels. *Rep.* 5168. US National Bureau of Standards.

Klemp, J. B., Rotunno, R. & Skamarock, W. C. 1997 On the propagation of internal bores. *J. Fluid. Mech.* **331**, 81–106.

Lilly, D. K. 1992 A proposed modification of the Germano subgrid scale closure method. *Phys. Fluids* A **4**, 633–635.

Mahesh, K., Constantinescu, G. & Moin, P. 2004 A numerical method for large eddy simulation in complex geometries, *J. Comput. Physics* **197**, 215–240.

Necker, F., Härtel, C., Kleiser, L. & Meiburg, E. 2005 Mixing and dissipation in particle-drive gravity currents. *J. Fluid Mech.* **545**, 339–372.

Ooi, S. K., Constantinescu, S. G. & Weber, L. 2007*a* A numerical study of intrusive compositional gravity currents. *Phys. Fluids* **19**, 076602. DOI: 10.1063/1.2750672.

Ooi, S. K., Constantinescu, G. & Weber, L. J. 2007*b* 2D Large Eddy Simulation of lock-exchange gravity current flows. *ASCE J. Hydraulic Engineering* **133**, 361–372. DOI: 10.1061/(ASCE)0733-9429(2007)133.9(1037).

Pierce, C. D. & Moin, P. 2001 Progress-variable approach for large-eddy simulation of turbulent cobustion. *Rep.* TF-80. Mechanical Engineering Department, Stanford University.

Pierce, C. D. & Moin, P. 2004 Progress-variable approach for large-eddy simulation of non-premixed turbulent combustion. *J. Fluid Mech.* **504**, 73–97.

Rottman, J. W. & Simpson, J. E. 1983 Gravity currents produced by instantaneous releases of a heavy fluid in a rectangular channel. *J. Fluid Mech.* **135**, 95–110.

Shin, J., Dalziel, S. & Linden, P. F. 2004 Gravity currents produced by lock exchange. *J. Fluid Mech.* **521**, 1–34.

Simpson, J. E. 1972 Effects of the lower boundary on the head of a gravity current. *J. Fluid Mech.* **53**, 759–768.

Simpson, J. E. 1997 *Gravity Currents: In the Environment and the Laboratory*, 2nd edn. Cambridge University Press.

Simpson, J. E. & Britter, R. E. 1979 The dynamics of the head of a gravity current advancing over a horizontal surface. *J. Fluid Mech.* **94**, 477–495.